SATELLITE DETECTABILITY MODELING FOR OPTICAL SENSORS

M.D. Hejduk
Titan Corporation, 480 Wooten Road, Colorado Springs, CO, 80916
J.V. Lambert
The Boeing Company, 1250 Academy Park Loop, Suite 110, Colorado Springs, CO, 80910
C.M. Williams
Consultant, Colorado Springs, CO
R.L. Lambour
Massachusetts Institute of Technology Lincoln Laboratory, 244 Wood Street, Lexington, MA, 02420

ABSTRACT

The movement to maintain the entire satellite catalogue with higher-order orbital theories has led to the commissioning of an appropriately-enhanced sensor tasking algorithm set, and among the improvements are more sophisticated satellite-sensor detectability calculations that go beyond mere geometry to consider target satellite characteristics and observing conditions at the sensor. AFSPC/XOCS, the sponsor for the new sensor tasker, asked Titan to act as lead developer for the new optical sensor satellite detectability models and algorithms for the sensor tasker. This paper describes the results of this development effort, which has yielded a new modeling approach to predict satellite brightnesses, using Kriging Optimized Interpolation; an algorithm to adjust site background sky brightnesses for anticipated lunar light pollution; a standardized procedure to calculate expected signal, noise, and probability of detection for the various optical sensors in the present SSN inventory; and a methodology for constructing tables of minimum observable brightnesses as a function of site background sky and target angular rate.

1. MODELED TARGET BRIGHTNESS

Illumination conditions for a satellite can be described in terms of three angles, shown diagrammatically in Fig. 1. The solar phase angle is the angle between the satellite-sun and satellite-sensor vectors. The aspect angle is the angle between the satellite-sun vector and the unit normal of the satellite's principal surface (or some other conveniently-chosen normal in the satellite's local coordinate system). The obliquity angle is the dihedral angle between the planes formed by the phase-angle vectors and the aspect-angle vectors. While the solar phase angle is easy to calculate, in general a satellite's aspect function is not known, leaving the latter two angles indeterminate. However, if it is known that a satellite maintains an invariant aspect with respect to a sensor (as is the case with geostationary satellites), then the only variation in the portion of the satellite illuminated is that due to changes in the solar declination; so the solar declination angle can serve as an adequate substitute for the aspect and obliquity angles. The two angles used in the proposed modeling were thus solar phase and declination angles.

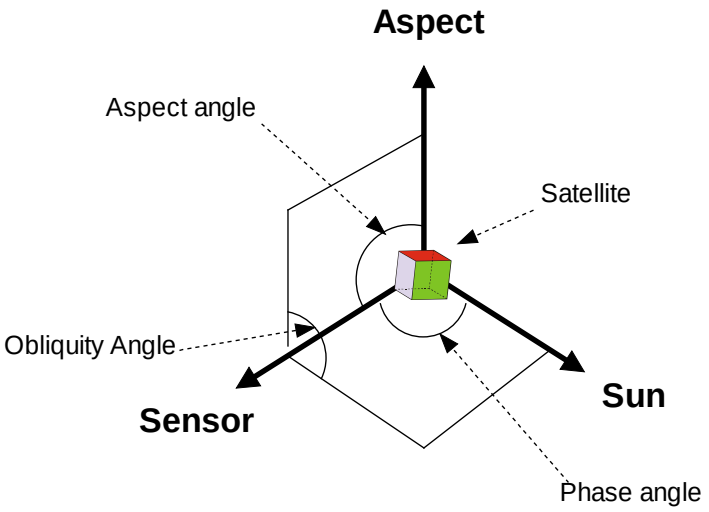

Fig. 1. Illumination angle definitions

In the initial publication of the Visual Magnitude Satellite Catalogue (version 1.0), a simple first-degree model in phase and declination was employed, whose appropriateness to solar phase angle was well attested [1, 2, 3, 4, 5] but which lacked any real pedigree for solar declination angle. A general second-degree model was used in a subsequent study [6]; and while in general improved performance was observed, there was still a substantial number of cases where its performance could not be called satisfactory. The difficulty in using a deterministic approach lies in selecting a functional form for the solar declination angle dependence, as this is governed nearly entirely by the configuration of the particular satellite and the observing site latitude; and in fact one may despair of finding an appropriate form for simply a notable minority of the satellite population, even when grouped by object type. This intractable problem with deterministic modeling leads one to consider stochastic alternatives, or at the least supplements.

Having examined the alternatives, it was decided to employ a technique, borrowed from geostatistics, called Kriging Optimized Interpolation. This technique is based on regionalized variable theory, in which a variable is seen to vary continuously in any given (spatial) neighborhood but not in a fully deterministic way. Many geological phenomena behave in this manner: the groundwater height at a given well location, for example, can be expected to be very similar to the groundwater height observed at a well a short distance away; as this distance is increased, the correlation will weaken until there is essentially no correlation at all. This same behavior is expected of satellite brightnesses: the brightness of a satellite at a given solar phase and declination angle is expected to correlate to the brightnesses at proximate phase and declination angles. The value of the method is to characterize the degree of correlation as a function of separation distance in the two parameters (phase and declination) and use these correlation data to construct a set of optimal (BLUE) weighting factors to apply when interpolating observed data to determine the expected brightness and its variance at a desired phase-declination "position." The theory of this technique is described quite capably in a full-length monograph [7] and its application to satellite brightness estimation in a previous conference paper [6], so little more need be said about it here other than that under controlled conditions it has been shown to be an effective technique for predicting satellite brightnesses given the desired solar phase and declination angles, even if these parameters fall outside the general range of observations. Next year Titan is planning to issue a report on how the technique has fared against both ground- and space-based observation catalogues and how well known difficulties, such as phase-declination anisotropy, have been addressed. The model produces solar-equivalent brightnesses in magnitude-space, normalized to an observing range of 36,000km, as a function of signed solar phase and declination angle.

2. VIEWING CONDITIONS AT THE CANDIDATE SITE

Observing range affects satellite brightness according to the inverse-square law, by which brightness intensity varies inversely with the square of the target-telescope separation distance. The standard correcting equation is given in (1); m_v is the brightness value obtained from the model, R is the range-to-target in the present observing situation, and R_0 is the VM catalogue nominal observing range of 36,000 km.

$$T_{vm} = m_v + 5Log_{10}(R/R_0) \tag{1}$$

Atmospheric extinction loss of satellite brightness is, to the first order, a function of the amount of the atmosphere transversed; and the thickness of the atmosphere is reasonably represented by the secant of the complement of the elevation angle, that is, the secant of the angular depression from zenith—this gives the number of airmasses that are penetrated, presuming a "flat earth" model that is can be used down to about fifteen degrees of elevation. Approximately 0.3 visual magnitudes are attenuated by each airmass (although this can become much worse in high humidity or light cloud cover) at 5000 Angstroms [8], producing an overall relationship of

$$\Delta M_v = 0.3\sec\xi\,, \tag{2}$$

where ξ is the depression angle from zenith. Atmospheric extinction is not actually wavelength-independent, but a full-spectrum treatment is adequate for the present application.

Lunar Light Pollution is one of the environmental effects on optical detectability that can be calculated and thus accounted for *a priori*. CCD cameras routinely calculate a background sky brightness value for each observing frame. With a repository of data of calculated background sky brightnesses and the knowledge of the observing geometry of the telescope at the time of calculation, one could construct a correlation relationship between background sky brightness and angular distance from the moon, further delineated by phase of moon and lunar elevation (lower lunar elevations will probably produce more scattering because of the greater atmospheric depth to penetrate). These data will soon be available from the three GEODSS sites and from RAVEN; and after sufficient data are assembled, a more sophisticated, site-specific lunar light pollution algorithm will be developed. However, in the absence of such data, it is necessary to rely on other small data captures and experiments in order to establish some version of the relation between background sky brightness and lunar phase and position. The procedure described here uses experimental data taken at the Cloudcroft, NM observing site in the early 1970's; while modest, these data are adequate to produce a reasonable first-order solution.

First, the brightness decrement, in Mv, of the moon at its particular phase was determined. The brightness decrement is the degree to which the moon's brightness is reduced as the lunar phase angle increases; while its range is in principle from 0 (full moon) to infinity (new moon), it can be *de jure* bottom-capped at 3.0 visual magnitudes (at phase angles greater than 90 degrees the lunar brightness is small enough to be considered negligible). The relationship, whose data come from [9], is shown, along with two quadratic fits, in Fig. 2. Fit #2 is the optimal fit, but Fit #1 is properly constrained to pass through the origin and has a nearly identical *F*-test value, so Fit #1 was the fit selected. The resulting fitting function against phase angle α is thus

$$\Delta M_v = 0.000176\alpha^2 + 0.0139\alpha \ . \tag{3}$$

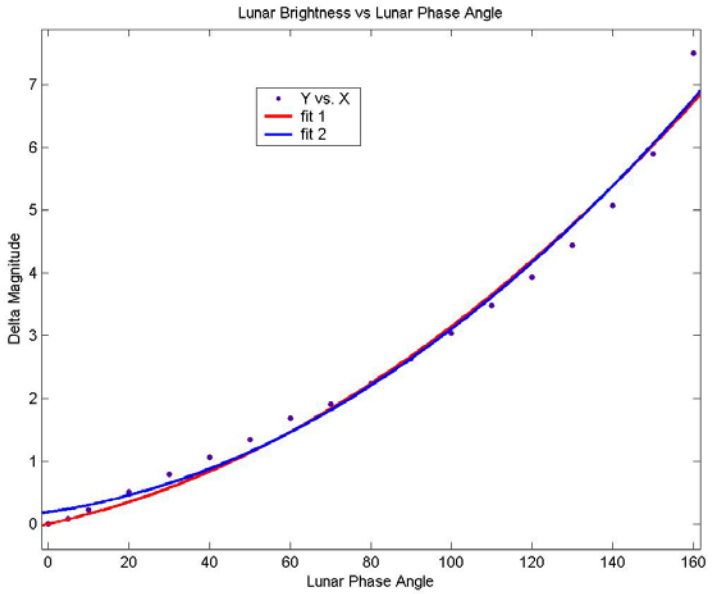

Fig. 2. Lunar brightness decrement versus lunar phase angle

Using the relationship given in (3), a background sky brightness vs. lunar brightness decrement relationship can be constructed for the Cloudcroft dataset; Fig. 3 shows these transformed data and their quite successful linear fit, producing the relation

$$B_{vm} = 1.58\Delta M_v + 17.39 \tag{4}$$

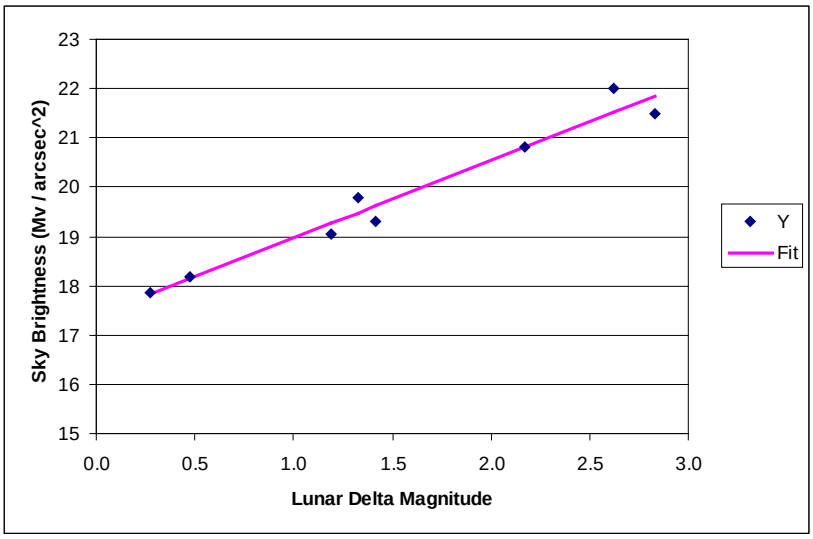

Fig. 3. Background sky brightness versus lunar brightness decrement for Cloudcroft site

One can expect the slope of this curve to be the same at any site, so all that remains is to translate the line in the manner dictated by the clear night, new moon background sky value ($\overline{B}_{vm}$) for the desired site. Because 3.0 delta magnitude was defined as the zero condition, the relation to determine the y-intercept *b* for a given site is given by

$$b = \overline{B}_{vm} - 3M \tag{5}$$

where M is the generic slope. Substituting back into (4), the consolidated formula is

$$B_{vm} = 1.58\Delta M_{v} + (\overline{B}_{vm} - 4.73) \tag{6}$$

Finally, the temporal aspect to this brightness adjustment, governed by how far moonrise or moonset has progressed, must be considered. This phenomenon was investigated at Cloudcroft, with Fig. 4 showing the relationship between background sky and hours after moonrise:

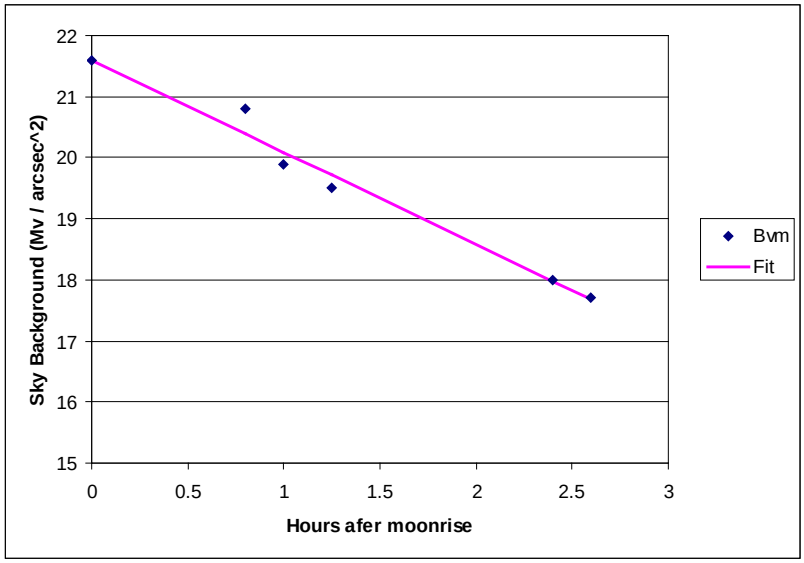

Fig. 4. Background sky brightness versus lunar presentation

After the 2.5 hour point, B_{vm} becomes essentially invariant with time; these invariant data points have been eliminated from the above graph and the linear fitting. This same rate of light pollution instantiation is expected, regardless of the ambient background sky or the moon phase; so all that is important from the relation is the slope of the line, which works out to be nearly exactly -0.4. The background sky brightness is thus given as a function of time as

$$\begin{aligned} B_{vm}(t) &= (B_{vm} - \overline{B}_{vm})(0.4t) + \overline{B}_{vm}; \quad t \le 2.5\, hrs \\ B_{vm}(t) &= B_{vm} \qquad\qquad\qquad\quad ; \quad t > 2.5\, hrs \end{aligned} \tag{7}$$

The inverse of this relation is to be followed 2.5 hours before moon-set.

3. SIGNAL, NOISE, AND SNR CALCULATIONS

The present procedure to determine the target signal and induced and ambient noise follows [10]. Nearly all the parameters are telescope- and camera-dependent.

The signal from the target, written as the number of photoelectrons per second $\dot{S}$, is given by

$$\dot{S} = A_{eff} \langle QE \rangle F0 10^{-0.4 T_{vm}} \tau_{atm} . \tag{8}$$

A_{eff} is the effective collecting area of the telescope (in m^2), easily calculated if the telescope effective diameter is known; <QE> is the solar-weighted quantum efficiency of the CCD, in photoelectrons per photon; F0 is the flux of a zero-magnitude target, in photons per square meter per second; T_{vm} is the apparent visual magnitude of the target, already corrected for observing range (produced by the model described in Section 1); and τ_{atm} is the atmospheric transmittance, here set to unity because the apparent visual magnitude has already been corrected for atmospheric attenuation (described in Section 2). This value indicates the total signal rate received across the detector.

One wishes next to determine the signal that falls on a single pixel (or pixel group), and a different approach is taken depending on whether the telescope is operating in rate-track or sidereal mode. In the rate track detection mode, the telescope is slewed at the same rate as the object, so the signal remains focused and integrated on a few contiguous pixels. In this case, the estimated object signal on the best pixel, measured in photoelectrons, during each individual frame is given by

$$S_T = \dot{S} T_{\exp} k_f , \tag{9}$$

where T_{exp} is the single-frame exposure time and k_f is the "straddle factor" which represents the expected fraction of the signal falling on the best pixel. It should be noted that the value of k_f depends on the distribution of the signal (or characteristic radius) as compared to the size of a pixel. A typical sensor might have a straddle factor of about 0.4, indicating that the best pixel will contain, on the average, approximately 40% of the total signal received. If a binned mode were used on this sensor, in which the signal from four continuous pixels is summed, the effective pixel area would be increased by a factor of four; and the associated straddle factor could be expected to increase to approximately 0.70.

For the sidereal detection mode, it is more difficult to estimate the signal in a pixel since it is distributed over all pixels along the streak. In this case, the estimated object signal in each streak pixel, measured in photoelectrons, is given by

$$S_T = \dot{S} T_{\exp} \sqrt{k} / p , \tag{10}$$

where T_{exp} is the exposure time of each of the individual frames, k_f is the straddle factor, and p is the length of the streak, in pixels, during each individual frame. The number of pixels in each frame of the streak is given by

$$p = \frac{\omega T_{\exp}}{\alpha}, \tag{11}$$

with ω defined as the object's angular rate (in arc-seconds per second) along its azimuth, $T_{\exp}$ as the frame exposure time, and α as the pixel's angular size in arc-seconds. In general, sidereal detection should only be used when p exceeds two pixels per frame. If p is less than unity, it should be set to unity to reflect the fact that falling within a single pixel is merely all of the available signal, not a fictitious increased amount of signal were the exposure time expanded to allow a full pixel to be crossed. Of course, as is common in signal processing, multiple frames may be taken by the sensor and "stacked" in order to increase the coherent gain.

Vacuum tube sensors include a (relatively wide) raster matrix as part of the tube assembly and therefore can be treated as the equivalent of CCDs with a very large straddle factor (close to 1, meaning that nearly all of the signal will fall within one raster box).

Induced noise arises from three basic sources: camera readout noise, noise produced by the background sky brightness, and "dark current" noise produced by the CCD chip. The total noise can be written as

$$\sigma = \sqrt{N_{sys}^2 + BT_{\exp} + \left(\eta_{QE} BT_{\exp}\right)^2 + N_{DC} T_{\exp} + \left(\eta_{DC} N_{DC} T_{\exp}\right)^2}, \tag{12}$$

in which N_{sys} represents the RMS system noise, in electrons; B the background sky photoelectron production rate, in photoelectrons per pixel per second, the precise calculation paradigm given in (13) below; η_{QE} the detector responsivity variation, in percent; N_{DC} the CCD dark current production rate, in electrons per pixel per second; and η_{DC} the RMS variation of the dark current production rate, in percent. The background photoelectron production rate B is calculated as follows:

$$B = \left(10^{-0.4 B_{vm}}\right) A_{eff} \langle QE \rangle F 0 \alpha^2, \tag{13}$$

in which B_{vm}, the background visual magnitude (calculated and modified as specified in Section 2), is given in m_{v} per square arc-second and α is the pixel size in arc-seconds. The remainder of the terms are defined as part of equation (8). Overall, this noise calculation approach underestimates the actual noise because it neither considers the additional noise due to streaked stars in the field of view (for the rate-track case) nor addresses the additional dark current that accrues in the frame-transfer area of the CCD while awaiting readout.

All species of noise produced by vacuum tubes are considerably larger than their counterparts in the CCD case. Because the values are so much larger, little loss of fidelity is introduced by failing to include the variance terms on dark current production and background sky noise. Additionally, system readout noise for tube sensors is reasonably approximated by the square root of the target signal.

With the signal and noise determined, the single-frame signal-to-noise ratio (SNR) is simply their ratio, converted to decibels if desired. Several relationships should be observed relating to signal to noise calculations. For the rate track detection method, when using frame stacking the target signal will increase linearly with the total exposure times, whereas the noise in the normal background pixel increases with the square root of the exposure times. Consequently, the SNR during rate track increases with the square root of the exposure time; the result is that longer total integration times result in the detection of dimmer objects, as one would expect. However, with sidereal detection methods, the relationships are much different. As in the case for rate track, the noise value increases as the square root of each exposure time. However, for longer exposure intervals, the streak becomes proportionally longer, but the signal in each pixel along a streak remains unchanged. Consequently, in sidereal tracking, the SNR for each pixel is inversely proportional to the square root of the single-frame exposure time. This is counterintuitive, but it means that longer single-frame exposure intervals generally result in decreased SNR. However, it does mean that if a camera can be operated in a binned mode and thus achieve a higher frame rate, the SNR may be increased.

4. TELESCOPE PARTICULARS, P_d, AND TABLES OF LIMITING BRIGHTNESS

Care must be exercised to determine and incorporate into the model each telescope's rule-base for determining its acquisition mode and governing parameters. A typical system that supports multiple acquisition modes varies these modes (*e.g.*, simple sidereal, binned-pixel sidereal, or rate-track), exposure time, and number of frames depending on the object's predicted brightness and angular rate. The following table gives some possibilities for this:

Table 1. Typical detectability modes

	Very Bright	**Normal**	**Dim**	**Very Dim**
Fast Objects	Sidereal Standard Tracklet	Sidereal Standard Tracklet – 2 x 2 Binned Pixels	Rate Track Standard Tracklet	Rate Track Modified Tracklet – increased exposure
Normal Objects	Sidereal Standard Tracklet	Sidereal Standard Tracklet	Rate Track Standard Tracklet	Rate Track Modified Tracklet – increased exposure
Slow Objects	Sidereal Modified Tracklet additional frames for streak construction	Sidereal Modified Tracklet – additional frames for streak construction	Sidereal Modified Tracklet – additional frames for streak construction	Sidereal Modified Tracklet – increased exposure

In contrast, some telescopes operate exclusively in rate-track mode when responding to tasking, taking single, long frames. At the beginning of each session, the analyst can configure the camera for either short- or long-exposure operations, although the long-exposure setting is the more commonly employed. Other telescopes utilize exclusively rate-tracking for tasking response but employ coherent integration to increase telescope sensitivity.

If the SNR is known, then the P_d can be determined by consulting tables of P_d as a function of SNR and false alarm rate; the difficulty, and to some degree arbitrariness, is in the judicious selection of the false-alarm rate. A false-alarm rate of 10^{-3} was chosen for the CCD automatic detection routines; these routines have proven to operate reliably, especially in sidereal mode, in which streak construction presents additional opportunities to identify and discard noise. A rate of 10^{-2} was selected for the tube sensors, which rely on an operator's viewing screen output and manually identifying the target, as analyst-directed detection continues to outperform even the better automated detection algorithms. The detection of a rectangular pulse in the presence of white noise was seen as the closest approximation to the present optical detection problem, and the particular contour plot used to determine P_d is provided in [11] and given below:

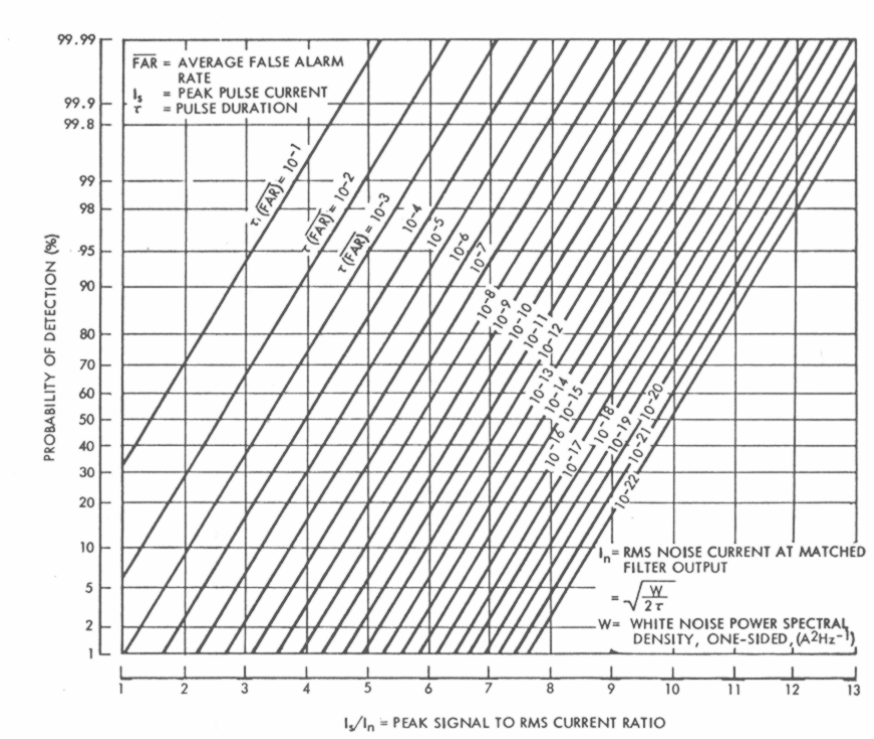

Fig. 5. P_d as a function of SNR and false alarm rate

For rate track processing, a dynamic thresholding process is used that requires the identification of adjacent pixels. To achieve this, it is estimated that a SNR of 8 might be required on the best average (central) pixel so that multiple adjacent pixels also pass thresholding; this should result in an P_d of about 0.95 for an object. It is also prudent in such situations to use a verification frameset; this is much like the use of detect and verify processing employed in radar processing.

When images are collected in the sidereal mode, the detection processing is significantly different. One does not need a P_d of 0.95 for each pixel along the streak. In fact, there may be tens or hundreds of pixels along a streak, and the streak may be apparent even if 50% or fewer of the pixels are thresholded. Results presented in [12] for the SBV sensor indicate that sidereal streaks can be detected with a P_d exceeding 0.95 even though the average streak pixel may have a SNR of 3 or less. If matched velocity filter processing were used on a sidereal frameset, objects should be detectable at an SNR of approximately 1; but this processing is very computationally intensive and is not generally used during real-time detection processing. It should be noted that one generally cannot calculate P_d directly as a function of SNR; these values and tables are usually derived from empirical data collected from real or simulated streak detection processing.

At this point two options present themselves for the routine determination of detectability of a particular satellite on a particular pass at a particular site: to use all that has been explained so far to calculate an explicit P_d for every such case, or to use this procedure to calculate tables of minimum detectable brightness as a function of satellite angular rate and background sky brightness. For the sensor tasking application, the choice is a difficult one. In trying to decide to which of several sensors to task an object for a particular day, the most straightforward way to effect a comparison among them is to calculate the P_d for each pass at each sensor and select the one with the highest predicted P_d. This approach, while the cleanest and yielding the least ambiguous adjudication among sensors, does introduce a specific disadvantage *vis-à-vis* minimum detectable brightness tables: it is much more difficult to refine with time. Most of the parameters that drive the signal and noise calculation are performance parameters of the CCD/tube that were only design parameters or performance estimates from analogous cases; and if they were in fact measured at some point, there is little hope of any field testing's being performed during each unit's operational life. The calculated P_d will thus be based in perpetuity on performance indices that are unvalidated design parameters or merely analogues from similar systems; and trying to reverse-engineer the parameters' actual values from tracking

data is truly not possible, as there are too many degrees of freedom in each equation. However, with new visual magnitude reporting standards that are presently being worked, empirical updates to detectability tables should be quite straightforward. The following table shows an example of the kind of data desired:

Table 2. Photometric data recording example

UTC Date_Time					Sat	Sens	Obs	Slant	Phase	Sky Bkg	Pos RA	Pos Dec	Rate RA	Rate Dec
Year	Day	Hr	Min	Secs	ID	ID	Vmag	Range (km)	Angle (deg)	mag	(deg)	(deg)	(deg/sec)	(deg/sec)
2004	100	3	39	10	33333	100	8.4	16928	-16.32	18.8	211.9854	-22.9852	0.0087	-0.0010
2004	100	3	39	20	33333	100	8.5	16928	-16.32	18.8	212.0387	-22.9906	0.0087	-0.0010
2004	100	3	39	30	33333	100	9.5	16976	-16.227	18.68	212.0925	-22.9956	0.0089	-0.0009

(note that the table includes a signed value for the solar phase angle; this is because asymmetric satellites in general present a different illuminated surface before and after minimum phase). Because the solar phase and declination angles (the latter in terms of the UTC date) are recorded, these data can feed the brightness modeling outlined in Section 1; but more importantly, because the observation angular rates and background sky brightnesses are recorded, these data can be used to update minimum detectable brightness tables empirically. Observed brightnesses for each angular rate – background sky brightness bin are collected, and a desired lower percentile (or perhaps parameterized function if the data follow a characterizable distribution) is used to set the minimum detectable brightness. Given the advantage of being to update these tables empirically, it is recommended that they, rather than explicit P_d calculations for each tracking situation, be used to determine detectability and thus sensor tasking assignments.

5. SUMMARY OF ENTIRE CALCULATION PROCEDURE

The logic flow of the proposed calculation approach for assessing detectability of a known target during a particular pass is here summarized. First, the predicted brightness of the target is determined from the model described in Section 1, as a function of the solar phase angle, declination angle (date), range to target, and topocentric elevation of the pass. Next, the background sky brightness is determined by beginning with the new moon nominal background sky value for the site and incorporating the lunar brightness decrement offset, as a function of lunar phase angle and time since lunar rise (or before lunar set). After this, the adjusted background sky brightness, in conjunction with the target angular rate, is used to determine the minimum detectable brightness for those observing conditions from calculated tables. Finally, the target's predicted brightness from the model can be compared to the minimum detectable brightness value from the table to determine whether the satellite is likely to be detected by that sensor during that pass. If more than one sensor shows promising detectability during the tasking run period, the more promising case(s) can be identified either by a greater number of detectable passes or by the greater differential between the expected brightness and the minimum detectable value.

6. REFERENCES

1. Hejduk, M.D., Kervin, P.W., Lambert, J.V., Stansbery, E.G., Africano, J.L, and Pearce, E.C., "Visual Magnitude Satellite Catalogue Release 1.0", 2001 AMOS Technical Conference, Maui HI, SEP 2001
2. Lambert, J.V., "Interpretation of Geosynchronous Satellite Phase Angle versus Magnitude Relationships", Contract F05603-90-C-0010 Specialized Data Report: MOTIF FY95-01, 30 NOV 1994.
3. Lambert, J.V., "Analysis of Magnitude versus Phase Angle Data for Two Classes of Deep Space Satellites", Contract F05604-95-C-9011 Specialized Data Report: MSSS FY96-04, 11 OCT 1996.
4. Lambour, R.L., "Phase Angle Dependence of Satellite Brightness Derived from Space-Based Visible Data", MIT/LL Project Report SPC-8, 20 FEB 2001.
5. Lambour, R.L. and Sayer, R.W., "ETS Measurements of Satellite Phase Curves at High Phase Angles", MIT/LL Project Report ETS-138, 12 SEP 02.
6. Hejduk, M.D., Lambert, J.V., Williams, C.M., and Lambour, R.L, "Improved Satellite Brightness Estimation Techniques", 2003 AMOS Technical Conference, Maui HI, SEP 2003
7. Kitanidis, P.K., *Introduction to Geostatistics: Applications to Hydrogeology*, Cambridge: Cambridge University Press, 1997.
8. Walker, G. *Astronomical Observations: An Optical Perspective*, Cambridge: Cambridge University Press, 1987. pp 46-48.

9. Allen, C.W., *Astrophysical Quantities, 3rd Edition*, London: Athlone Press, 1973.
10. Rork, E.W. and Opar, T.P., "Processing and Analysis for Space Surveillance Capability of the Lincoln Front-Illuminated Quad CCD Imager," MIT/LL Technical Report ETS-89, 15 SEP 1990.
11. RCA Electro-Optics Handbook, Technical Series EOH-11, 1974.
12. Chu, P.L., "Efficient Detection of Small Moving Objects", MIT/LL Technical Report 846, 21 JUL 89.